

# Spatiotemporal signal propagation in complex networks

Chittaranjan Hens<sup>1,2,3</sup>, Uzi Harush<sup>1,3</sup>, Simi Haber<sup>1</sup>, Reuven Cohen<sup>1\*</sup> and Baruch Barzel<sup>1,2\*</sup>

**A major achievement in the study of complex networks is the realization that diverse systems, from sub-cellular biology to social networks, exhibit universal topological characteristics. Yet, such universality does not naturally translate to the dynamics of these systems, as dynamic behaviour cannot be uniquely predicted from topology alone. Rather, it depends on the interplay of the network's topology with the dynamic mechanisms of interaction between the nodes. Hence, systems with similar structure may exhibit profoundly different dynamic behaviour. We therefore seek a general theoretical framework to help us systematically translate topological elements into their predicted dynamic outcome. Here, we offer such a translation in the context of signal propagation, linking the topology of a network to the observed spatiotemporal spread of perturbative signals across it, thus capturing the network's role in propagating local information. For a range of nonlinear dynamic models, we predict that the propagation rules condense into three highly distinctive dynamic regimes, characterized by the interplay between network paths, degree distribution and the interaction dynamics. As a result, classifying a system's intrinsic interaction mechanisms into the relevant dynamic regime allows us to systematically translate topology into dynamic patterns of information propagation.**

Networks represent a powerful tool to visualize and predict information propagation in complex systems, from viral spread<sup>1</sup>, to neuronal<sup>2</sup> or biochemical<sup>3–5</sup> signals. In some cases the network topology exposes the natural geometry of the propagation, with the more distant nodes impacted at later times. In others, however, the translation is less transparent, a consequence of the diverse forms of nonlinear interactions that may take place between the nodes<sup>6–11</sup>. Therefore, advances are often system dependent, with each dynamics warranting its own dedicated analysis, allowing limited insight to transfer across domains.

To overcome this diversity we seek general tools to translate a network's topology into predictions on its observed propagation patterns—often characterized through the system's response to local perturbations<sup>3,12,13</sup>. A single component is perturbed, and as a result all other network components are impacted, leading, in the long term, to a cascade of responses, whose size and penetration depth help characterize the network's dynamic behaviour<sup>3,4,14,15</sup>. Such predictions, however, tracking the system's long-term response, provide little insight into its temporal propagation, leaving open time-related questions, such as, how much time it will take the cascade to build up, which nodes respond first and which later, or what percentage of nodes are impacted at any given point in time.

We address these questions here by predicting an individual node's degree-dependent response time, allowing us, by piecing together all local responses, to predict the complete network spatiotemporal propagation patterns. Analytically tractable for a family of commonly encountered steady-state dynamics, our formalism allows us to systematically translate topology into signal propagation, in effect, reestablishing networks as predictors of information spread.

## Diversity in signal propagation

To illustrate the challenge we begin with an artificial  $N$ -node protein interaction network  $A_{ij}$ , which we use to simulate the propagation

of biochemical signals in a sub-cellular environment (Fig. 1a). Denoting the abundance of the  $i$ th protein by  $x_i(t)$ , we capture the system's dynamics through<sup>16</sup>  $\dot{x}_i = -B_i x_i^a + \sum_{j=1}^N A_{ij} \mathcal{H}(x_j)$ , in which the first term describes a protein's self-dynamics, for example, degradation ( $a=1$ ), dimerization ( $a=2$ ) or a more complicated chain reaction (fractional  $a$ , Supplementary Section 2.2), and the second term depicts  $i$ 's regulation by its interacting partners, often captured by a Hill function of the form<sup>17,18</sup>  $\mathcal{H}(x_j) = x_j^h / (1 + x_j^h)$  (Fig. 1b). Changes in the abundance of one protein propagate, through  $A_{ij}$ , to affect the abundance levels of all other proteins, representing a spread of biochemical information in the system<sup>3</sup>. Hence we initiate a biochemical signal by introducing a perturbation  $\Delta x_j$  to the steady-state abundance of the source  $j$  (black node), and then track its propagation, as it penetrates the network, for illustration, focusing on four selected target nodes  $i=1, 2, 3, 4$  (coloured nodes).

In Fig. 1d–i we track the resulting propagation under different dynamics, by controlling the values of  $a$  and  $h$  and monitoring the sequence of responses  $\Delta x_i(t)$  of the four selected target nodes. We also measured the propagation times  $T(j \rightarrow i)$  for the signal in  $j$  to travel to  $i$  through

$$\Delta x_i(t = T(j \rightarrow i)) = \eta \Delta x_i(t \rightarrow \infty) \quad (1)$$

namely  $T(j \rightarrow i)$  represents the time when  $i$  has reached an  $\eta$ -fraction of its final response to the  $j$ -signal (typically setting  $\eta \sim 1/2$ , the half-life of  $i$ 's response; Fig. 1c, Supplementary Section 3.2). For  $a=h=1$  the propagation seems predictable—first impacting the nearest neighbours 1, 2, then reaching the farther nodes 3, 4 (Fig. 1d,e). This clean picture, however, is violated as the dynamics is changed. For instance, under  $a=1/2$  we find that the nearest neighbour 1 is impacted significantly later than all other nodes, seemingly skipped over by the more distant 3 and 4 (Fig. 1f,g). The opposite occurs when we set  $a=3, h=1/2$ , as now 1 becomes the first to receive the signal, preceding 4 by two orders of magnitude (Fig. 1h,i).

<sup>1</sup>Department of Mathematics, Bar-Ilan University, Ramat-Gan, Israel. <sup>2</sup>Physics and Applied Mathematics Unit, Indian Statistical Institute, Kolkata, India.

<sup>3</sup>These authors contributed equally: Chittaranjan Hens, Uzi Harush. \*e-mail: [baruchbarzel@gmail.com](mailto:baruchbarzel@gmail.com)

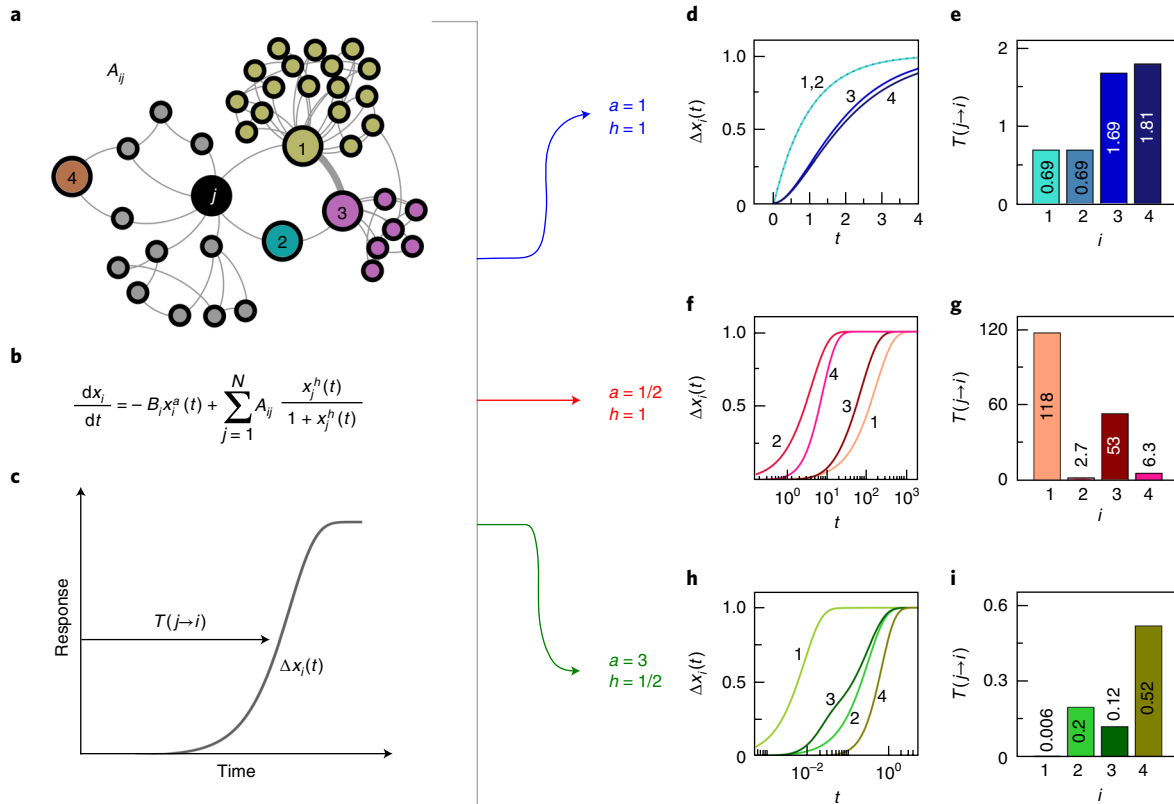


**Fig. 1 | Propagation of signals in a complex network environment.** To model network dynamics we use a two-layer description. **a**, The first layer is the topology, captured by the weighted network  $A_{ij}$ . **b**, The second layer is the system's dynamics, designed to capture the inner mechanisms driving the system's observed behaviour. Here, for illustration, we consider protein interactions in sub-cellular networks: proteins are depleted at a rate proportional to  $x_i^a$  (setting  $B_i=1$  for all  $i$ ) and activated by their network neighbours via the Hill function  $H(x_j) = x_j^h / (1+x_j^h)$  (refs. <sup>17,18</sup>). The dynamic behaviour of the system (**a,b**) can be captured through its patterns of information, or signal, propagation. A local signal in the form of an activity perturbation  $\Delta x_i$  applied to the source node  $j$  (black), spreading through the network to impact all other nodes  $1, 2, \dots$ . **c**, The spatiotemporal propagation of this signal is captured by the response of all target nodes,  $i$ , via  $\Delta x_i(t)$ , which we normalize to satisfy  $\Delta x_i(t \rightarrow \infty) = 1$ . The propagation time,  $T(j \rightarrow i)$ , captures the time for  $\Delta x_i$  to reach an  $\eta$ -fraction of its final response, here illustrated for  $\eta=1/2$  (half-life). We tested the propagation from  $j$  under different dynamics, varying the exponents  $a$  and  $h$ . **d**, The response  $\Delta x_i(t)$  versus  $t$ , as obtained for  $a=h=1$  for nodes  $i=1, 2, 3$  and  $4$  (coloured in  $A_{ij}$ ). 1 and 2 respond almost simultaneously, hence their overlapping plots. **e**, The propagation time  $T(j \rightarrow i)$  for these four nodes. As expected we find that the signal first reaches the neighbouring nodes 1, 2, then propagates to impact the next neighbours 3, 4. **f,g**, Changing the value of  $a$  to  $1/2$  has a pronounced impact on the propagation pattern, as now 1 seems to be skipped by the more distant 3 and 4. Moreover,  $T(j \rightarrow 1)$  is now two orders of magnitude greater than  $T(j \rightarrow 2)$ , despite being at equal distance from  $j$ , and in sharp contrast with their previously simultaneous responses. **h,i**, The propagation sequence is further scrambled under  $a=3, h=1/2$ , as are the propagation timescales, with 1 now preceding the others by two orders of magnitude. Hence,  $A_{ij}$  alone is insufficient to predict information spread, as indeed, changes in the dynamic equation in **b** translate to profound and seemingly unpredictable consequences on the observed propagation.

This diversity of propagation patterns is also expressed by the mean propagation time

$$\langle T \rangle = \frac{1}{N^2} \sum_{i,j=1}^N T(j \rightarrow i) \quad (2)$$

capturing the typical time for signals to cover the entire network. We find that  $\langle T \rangle$  ranges from  $\sim 10^{-2}$  (Fig. 1*i*, green) to  $\sim 10^2$  (Fig. 1*g*, red), representing a several order of magnitude difference in timescales exhibited by the same network. Consequently, signal propagation cannot be mapped directly to the network topology, as, indeed, even in this simple example, we observe that changes to the dynamics (values of  $a$  and  $h$ ) can have dramatic consequences on the spreading behaviour.

To advance from this anecdotal observation towards a general signal propagation framework, we seek to separate the role of the topology from that of the dynamics. Therefore, we constructed a systematic testing ground combining a diverse body of model and

empirical networks with a set of frequently encountered dynamic models. This includes Erdős-Rényi (ER) and scale-free (SF) networks<sup>19</sup> with different link weight distributions (SF, SF1, SF2), as well as empirical networks from social<sup>20–22</sup>, biological<sup>23–24</sup>, neuronal<sup>25</sup> and ecological<sup>26</sup> domains. To scan the dynamics space, we implemented relevant steady-state dynamic models, capturing epidemic spreading (E<sup>27</sup>), ecological interactions (M<sup>10</sup>), regulatory dynamics (R<sub>P</sub>, R<sub>2</sub><sup>17,18</sup>), neuronal activation (N<sup>28</sup>) and population dynamics (P<sup>29</sup>), together a spectrum of nonlinear models from diverse application fields. We arrive at a combination totaling 41 systems—each pairing a network with its relevant dynamics, on which to observe and understand the potential signal propagation patterns (Fig. 2a,b).

Introducing permanent activity perturbations  $\Delta x$  around the steady state, as in Fig. 1, we examined signal propagation in each of our 41 combined networks/dynamics. The results for SF, across all six dynamic models, are presented in Fig. 3a–f. We find that despite the fact that the networks and layouts in all panels are identical, the spatiotemporal propagation patterns are visibly different, depending on the type of dynamics: in some cases propagating,

expectedly, from core to periphery ( $\mathbb{R}_1, \mathbb{N}$ , blue), in others, strikingly, advancing from the periphery inwards ( $\mathbb{R}_2, \mathbb{P}$ , red) and finally, in  $\mathbb{M}$  and  $\mathbb{E}$ , featuring a seemingly random scatter of early responding nodes (green). These observations indicate a non-trivial interplay between structure and dynamics, whose mathematical roots we investigate below.

### Analytical framework for spatiotemporal propagation

To understand the roots of the observed propagation patterns we develop a unified framework to capture the behaviour of all dynamic models used in Figs. 1–3. Therefore we consider the general equation (Fig. 2c)

$$\frac{dx_i}{dt} = M_0(x_i(t)) + \sum_{j=1}^N A_{ij} M_1(x_i(t)) M_2(x_j(t)) \quad (3)$$

in which the nonlinear functions  $\mathbf{M} = (M_0(x), M_1(x), M_2(x))$  can be selected to cover each of the systems included in our testing ground (Fig. 2a,b), together with a range of additional social<sup>30</sup>, biological<sup>16</sup> or technological<sup>31</sup> dynamics. For instance, the regulatory models  $\mathbb{R}_1, \mathbb{R}_2$  are covered by equation (3) through  $\mathbf{M} = (-Bx^\alpha, 1, x^\beta/(1+x^\beta))$ ; similarly, the SIS model  $\mathbb{E}$  maps to  $\mathbf{M} = (-Bx, 1-x, x)$ ; excluded, however, are non-factorizable interactions, for example,  $M(x_i, x_j) = M(x_j - x_i)$  (ref. <sup>32</sup>). The network  $A_{ij} \geq 0$  represents a random weighted network, with arbitrary degree/weight distributions—that is, a positive weighted configuration model network<sup>33</sup>.

To predict the signal propagation patterns of equation (3), we first focus on each node's individual response time  $\tau_i$  to a directly incoming signal; that is, we seek the  $T(j \rightarrow i)$  for signals originating in  $i$ 's nearest neighbour  $j$ . In Supplementary Section 1 we show, based on linear response theory, that we can link  $\tau_i$  to  $i$ 's weighted degree  $S_i = \sum_{j=1}^N A_{ij}$  through the universal scaling relationship

$$\tau_i \sim S_i^\theta \quad (4)$$

where

$$\theta = -2 - \Gamma(0) \quad (5)$$

The parameter  $\Gamma(0)$  is determined by the system's dynamics  $\mathbf{M}$  through the leading powers of the Hahn series expansion

$$Y(R^{-1}(x)) = \sum_{n=0}^{\infty} C_n x^{\Gamma(n)} \quad (6)$$

where  $Y(x) = (d(M_1 R)/dx)^{-1}$ ,  $R(x) = -M_1(x)/M_0(x)$  and  $R^{-1}(x)$  denotes its inverse function. The Hahn expansion in equation (6) is a generalization of the Taylor expansion, to include both negative and real powers<sup>34</sup>; hence  $\Gamma(n)$ ,  $n = 0, \dots, \infty$ , represents a sequence of real powers in ascending order; that is,  $\Gamma(n+1) > \Gamma(n)$ . Equation (5) relates the exponent  $\theta$  in equation (4) to the leading power  $\Gamma(0)$  of equation (6), hence directly linking  $\tau_i$  to the system's dynamics  $\mathbf{M}$  (see Supplementary Section 2 for detailed application of equations (4)–(6) on all dynamics of Fig. 2b).

Equations (4)–(6) represent our first key prediction, showing that the individual response times of all nodes are driven by the interplay between topology,  $S_i$ , and dynamics,  $\theta$ . Therefore, the exponent  $\theta$  helps translate topology into dynamic insight, here mapping response time, a desirable dynamic function, to the weighted degree, a well-mapped topological characteristic. To test this prediction, we measured  $\tau_i$  versus  $S_i$  for each of the 41 systems summarized in Fig. 2a. The results, presented in Fig. 4a–c, fully confirm our predicted scaling: for  $\mathbb{R}_1$  and  $\mathbb{N}$ , equation (5) predicts  $\theta = 0$  (Fig. 4a); for  $\mathbb{R}_2$  and  $\mathbb{P}$ , it predicts  $\theta = 3/2$  and  $1$ , respectively (Fig. 4b);

for  $\mathbb{M}$  and  $\mathbb{E}$  the prediction is  $\theta = -1$  (Fig. 4c), all corroborated by our simulation results.

Most crucially,  $\theta$  is intrinsic to the system's dynamics  $\mathbf{M}$ , independent of the network topology  $A_{ij}$ . Indeed, Fig. 4a–c groups together distinct systems based on their shared dynamics:  $\mathbb{R}_1$  and  $\mathbb{N}$  having  $\theta = 0$ ,  $\mathbb{R}_2$  and  $\mathbb{P}$  with  $\theta = 3/2$  and  $1$ , respectively, and  $\mathbb{M}$  and  $\mathbb{E}$  both having  $\theta = -1$ . In each of these dynamic classes, the scaling of equation (4) is sustained across diverse networks, ranging in size, density and structural heterogeneity. Hence  $\theta$  is a fingerprint of the system's dynamic model  $\mathbf{M}$ , providing the desired separation of topology versus dynamics:  $A_{ij}$  provides the degrees  $S_i$  and their distribution  $P(S)$ , while  $\mathbf{M}$  translates these into  $\tau_i$  through  $\theta$  (Fig. 2d).

### Global propagation regimes

Equation (4) provides not only the local response times  $\tau_i$ , but also helps unravel the global propagation patterns  $T(j \rightarrow i)$ , predicting three distinct propagation regimes:

**Distance-limited propagation ( $\mathbb{R}_1, \mathbb{N}$ , blue).** In case  $\theta = 0$  we have  $\tau_i$  in equation (4) independent of  $S_i$ . Therefore, as the signal propagates along network paths, each node in its trajectory causes, on average, the same delay, and hence the propagation time  $T(j \rightarrow i)$  is primarily governed by the path length  $L_{ij}$ . In Fig. 4d we present  $T(j \rightarrow i)$  versus  $L_{ij}$ , confirming our prediction that in  $\mathbb{R}_1$  and  $\mathbb{N}$  propagation is, indeed, driven by distance.

**Degree-limited propagation ( $\mathbb{R}_2, \mathbb{P}$ , red).** For  $\theta > 0$  equation (4) predicts that hubs respond at a slower rate than low-degree nodes, in effect being the bottlenecks of signal propagation. In this class the length of a path  $L_{ij}$  is of little importance compared to the degrees of the nodes along its trajectory; especially in SF networks, where paths are extremely short<sup>35</sup>, whereas degrees range over orders of magnitude (Fig. 4e).

**Composite propagation ( $\mathbb{E}, \mathbb{M}$ , green).** For  $\theta < 0$  the hubs respond rapidly, and hence signal propagation is, again, primarily limited by the path length from source to target (Fig. 4f); however paths enriched with hubs will support a more rapid propagation.

We can now revisit the illustrative Fig. 1, to better understand its observed  $T(j \rightarrow i)$ . The blue dynamics (Fig. 1d,e) is distance limited ( $\theta = 0$ ), therefore the signal reaches the nearest neighbours first at  $t \approx 1$ , then proceeds to impact the next neighbours at  $t \approx 2$ . In contrast, red (Fig. 1f,g) is degree limited ( $\theta = 2$ ), and hence the highly connected hub node 1 is the last to receive the signal, bypassed by 3, whose incoming information is routed via the low-degree, and thus fast-responding, node 2. This illustrates that under degree-limited propagation, short paths do not necessarily translate to rapid propagation. Finally, for the green system (Fig. 1h,i), we predict  $\theta = -2/3$ , a composite dynamics, in which the hub-enriched paths are now fastest, leading to a third propagation sequence 1, 3 (hubs), followed by 2, 4.

Consequently,  $\theta$  provides not only local insight, but also guidelines on the global spreading patterns, identifying rapid versus slow pathways. More broadly, these insights can help us uncover the dynamic consequences associated with two of the most profound characteristics of real networks: first, most real networks exhibit extremely short paths, often following  $\langle L_{ij} \rangle \sim \log N^{35}$ ; second, the (weighted) degree distribution  $P(S)$  of many real systems is fat-tailed, often scale-free, featuring hubs alongside low-degree nodes<sup>36</sup>. Our analysis indicates that these two topological hallmarks impact the propagation of signals in a rather distinctive fashion. Whereas the short paths accelerate propagation, the impact of degree heterogeneity depends on the dynamic regime: hubs may either expedite propagation ( $\theta < 0$ , green, Fig. 4i), have no effect on it ( $\theta = 0$ , blue, Fig. 4g) or cause delays ( $\theta > 0$ , red, Fig. 4h).

To quantify this effect consider again the mean propagation time  $\langle T \rangle$  in equation (2), which measures the efficiency of the

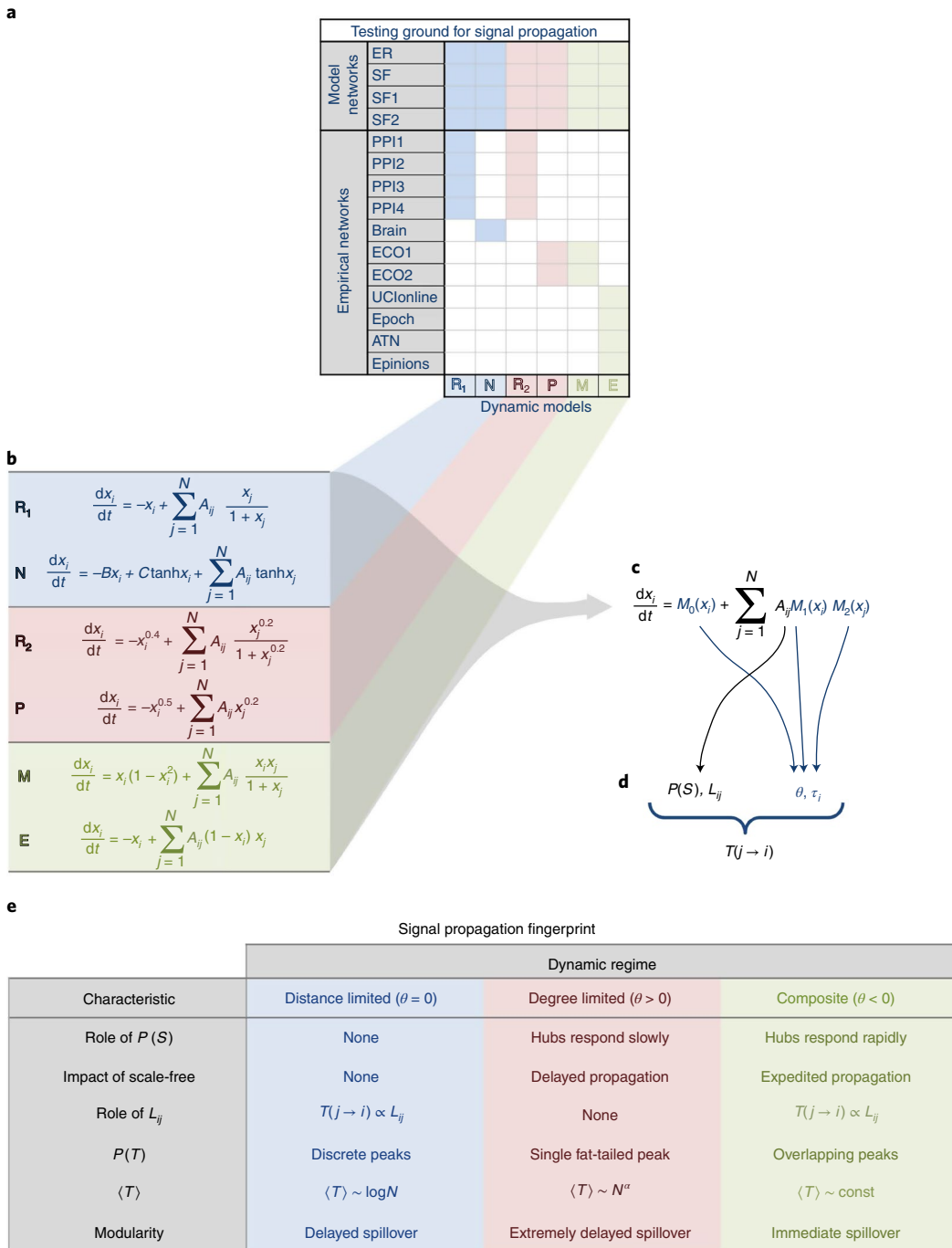


**Fig. 2 | Testing ground and characterization of network signal propagation.** **a**, We tested signal propagation on 41 systems constructed from combinations of 15 networks and 6 relevant dynamic models; for example, epidemic spreading **E** on the social network UClonline (shaded boxes). The networks (Supplementary Section 3.4): ER, Erdős-Rényi; SF, SF1, SF2, scale-free networks with binary, uniform and scale-free distributed weights, respectively; PPI1–PPI4, protein interaction networks<sup>22–24</sup>; Brain, physical connections between human brain regions<sup>38</sup>; ECO1/2, plant pollinator network of Carlinville, Illinois<sup>26</sup>, collapsed on to the plants/pollinators; UClonline, Epoch, Epinions and ATN, online social networks<sup>20–22</sup>. We tested all dynamic models on our four model networks (24 shaded boxes, top) and on the appropriate empirical networks (17 shaded boxes, bottom). **b**, The dynamics (Supplementary Section 2): **R<sub>1</sub>**, **R<sub>2</sub>**, gene regulation via the Michaelis-Menten model<sup>17,8</sup> with different exponents<sup>39</sup> for the self-dynamics (1 versus 0.4) and for the regulating Hill function (1 versus 0.2); **N**, activation dynamics between brain regions<sup>28</sup>; **P**, population dynamics through birth-death processes<sup>29,31,40</sup>; **M**, mutualistic interactions, for example, plant-pollinator relationships in ecological networks<sup>10</sup>; **E**, susceptible-infected-susceptible (SIS) model for epidemic spreading<sup>41–43</sup>. **c**, We offer to capture these dynamics, together with a range of additional pairwise dynamics, through the universal equation (3). **d**, The propagation patterns emerge from the interplay between the weighted topology  $A_{ij}$  and the system's intrinsic dynamics  $\mathbf{M} = (M_0(x), M_1(x), M_2(x))$ . The topology provides the path lengths  $L_{ij}$  and the weighted degree distribution  $P(S)$ ; the dynamics determine how these topological features translate into  $\tau_i$  through  $\theta$  (equation (4)). Combining the two contributions, for example, equation (7), provides the spatiotemporal propagation  $T(j \rightarrow i)$ . **e**, Depending on the value of  $\theta$  we predict that systems within equation (3) exhibit three dynamic regimes, each with its series of distinctive observable fingerprints, characterizing how topological features (for example, system size  $N$ ), impact propagation patterns (for example, mean propagation time  $\langle T \rangle$ ; characteristic 5).

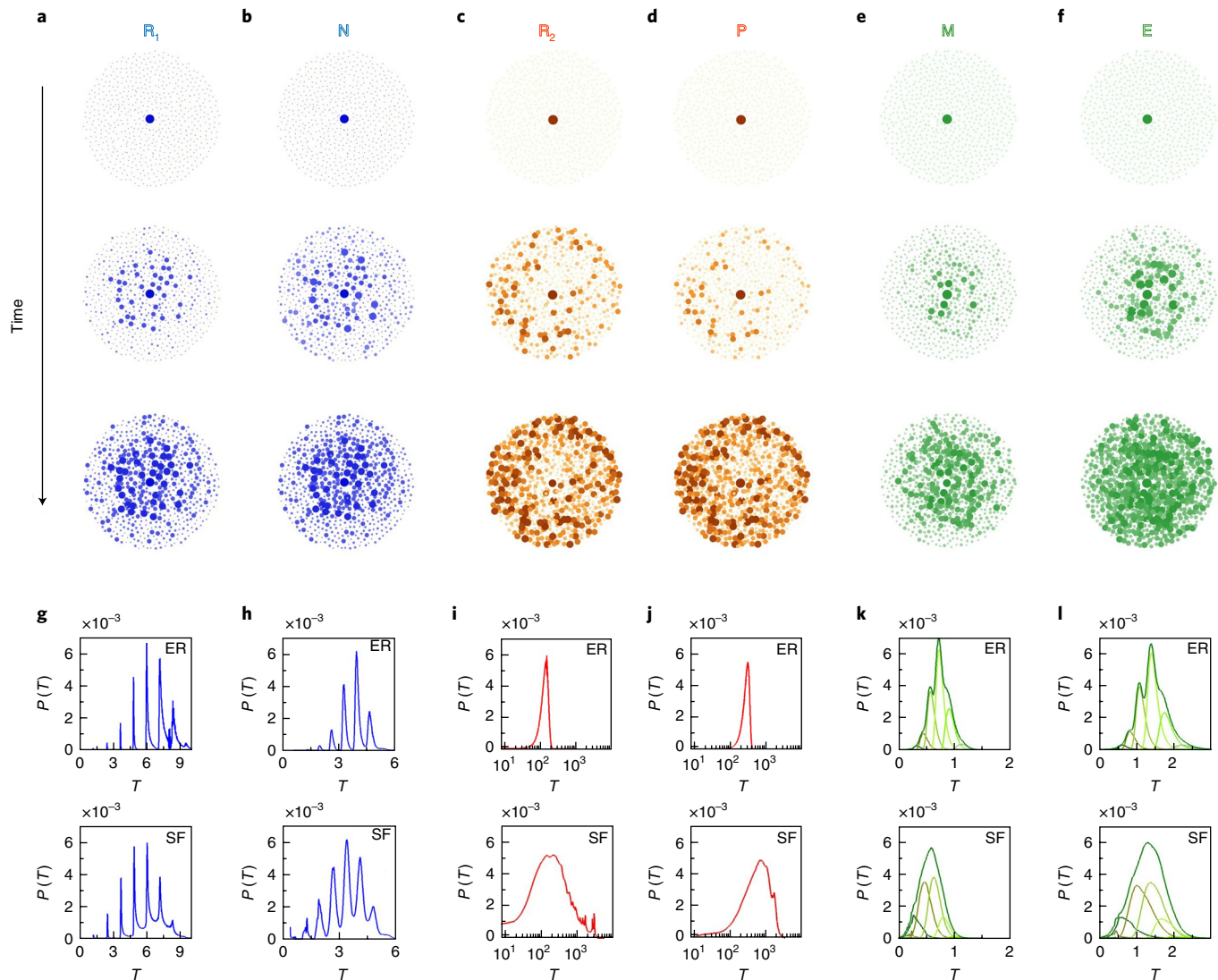


**Fig. 3 | Classifying the zoo of propagation patterns.** **a**, Propagation on the scale-free network SF under regulatory dynamics  $\mathbb{R}_1$ . At  $t=0$  we introduce a perturbation to the activity of a randomly selected source node (centre), then track the propagation, presenting three snapshots observed at selected time points. The size and colour depth of each node represent its response; hence nodes that received the signal at earlier times appear first. **b–f**, We repeated this experiment on the same network and the same source node, using different dynamic models (as detailed in Fig. 2b). We observe different propagation patterns depending on the dynamics, resulting in a zoo of seemingly unpredictable propagation patterns. **g,h**, The probability density function  $P(T)$  versus  $T$  as obtained from  $\mathbb{R}_1$  and  $\mathbb{N}$  on ER (top) and SF (bottom). We find that  $P(T)$  exhibits multiple sharp peaks in both ER and SF, indicating that the degree distribution  $P(S)$  has little impact on the propagation. **i,j**, In  $\mathbb{R}_2$  and  $\mathbb{P}$  the density  $P(T)$  has a fundamentally different form with no discrete peaks. Here  $P(T)$  is broader in SF (bottom) compared with ER (top), showing that now  $P(S)$  has a significant impact on the propagation. **k,l**,  $\mathbb{M}$  and  $\mathbb{E}$  exhibit a third type of  $P(T)$ , featuring multiple overlapping peaks. To highlight these peaks we show (in shades of green)  $P(T \cap L)$ , capturing the probability that  $T(j \rightarrow i) \in (T, T+dT)$  while  $L_{ij} = L$ ; that is,  $P(T)$  extracted exclusively from node pairs at distance  $L_{ij} = 1, 2, \dots$ . The complete  $P(T)$  is a composition of these overlapping peaks. For SF (bottom) the inner peaks  $P(T \cap L)$  are broader and hence show more overlap compared with ER (top). Therefore in this class the propagation is affected both by distance (discrete peaks) and by  $P(S)$  (variance within each peak). Complementary results from all our 41 model/empirical systems—the testing ground of Fig. 2—appear in Supplementary Section 4.

network propagation. Our analysis predicts three levels of efficiency. The first, efficient spread ( $\theta=0$ ,  $\mathbb{R}_1, \mathbb{N}$ , Fig. 4j), occurs in distance-limited propagation where we have  $T(j \rightarrow i) \propto L_{ij}$  and hence, for a random network  $\langle T \rangle \propto \langle L_{ij} \rangle \sim \log N$ , a rapid coverage that grows only logarithmically with the system's size. The second, slow spread ( $\theta>0$ ,  $\mathbb{R}_2, \mathbb{P}$ , Fig. 4k), occurs in the degree-limited regime where the propagation times are governed by the hubs, whose degrees increase with  $N$ ; hence for a large system ( $N \rightarrow \infty$ ), signals require an extremely long time to penetrate the network. For SF networks this leads to a scaling behaviour  $\langle T \rangle \sim N^\alpha$ , an inefficient propagation in which  $\langle T \rangle$  diverges polynomially with  $N$ . Therefore, despite the fact

that SF shrinks the topological distance, it greatly inflates the temporal distance, illustrating the potentially non-trivial mapping from topology to dynamics. Finally, in composite dynamics ( $\theta<0$ ,  $\mathbb{E}, \mathbb{M}$ , Fig. 4l), signals rapidly propagate thanks to the hubs. Consequently, the propagation time is primarily determined by the response of the target nodes, which is independent of  $N$  or of the path length. This results in an ultra-efficient spread, in which  $\langle T \rangle \sim \text{const}$ , effectively independent of  $N$ . Indeed, in Fig. 4l we find that networks of vastly different size, ranging over more than four orders of magnitude, are all covered within approximately the same  $\langle T \rangle$ ; a counter-intuitive form of propagation, that is yet fully predicted by our formalism.

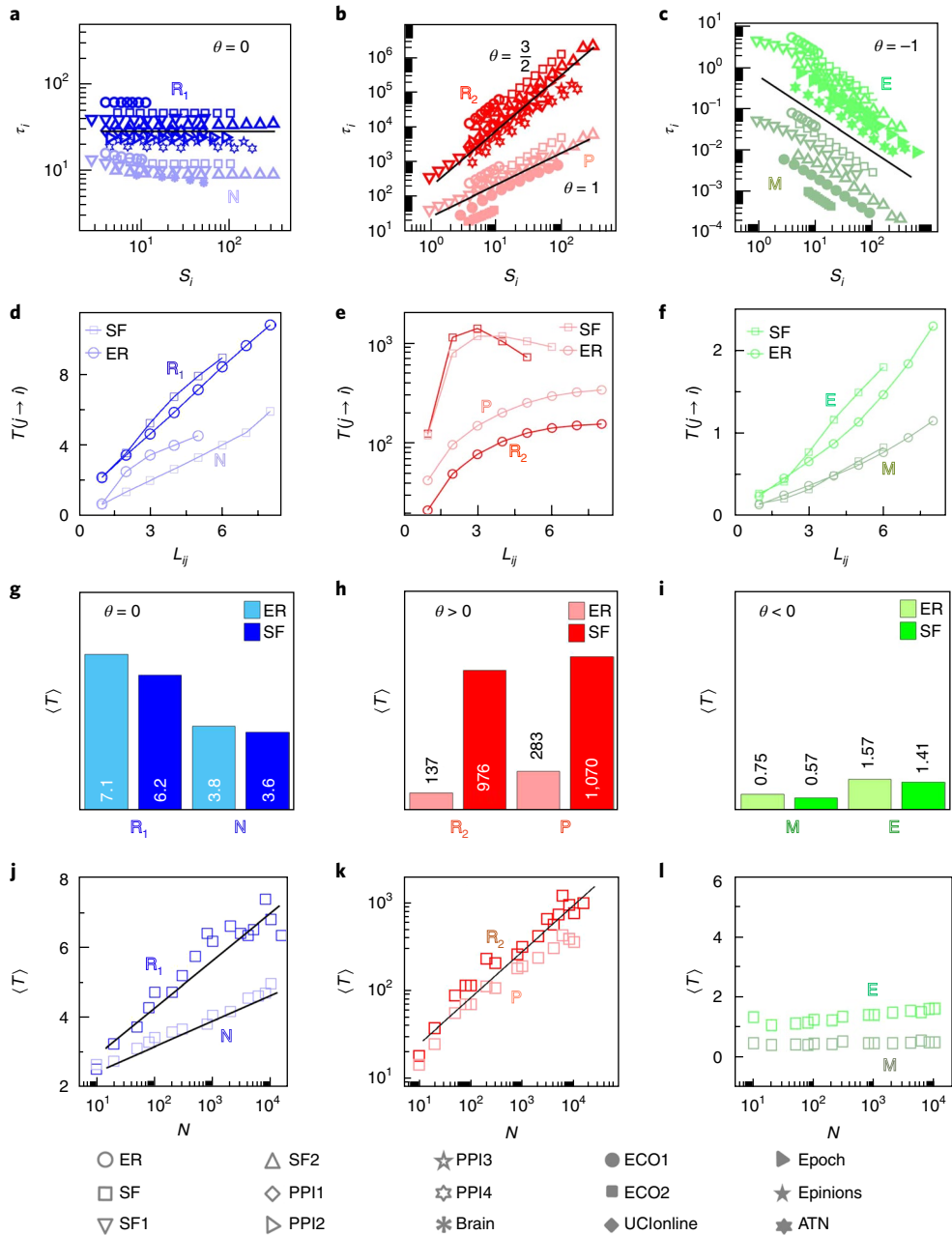


**Fig. 4 | Dynamic regimes of signal propagation.** We measured the local response times  $\tau_i$  of all nodes versus their weighted degree  $S_i$  for our 41 networks/dynamics detailed in Fig. 2a,b. **a**,  $\tau_i$  versus  $S_i$  as obtained from  $\mathbb{R}_1$  (dark) and  $\mathbb{N}$  (light) on all relevant networks (symbols). As predicted, we observe the scaling of equation (4) with  $\theta=0$  (solid black line). This scaling relationship is independent of  $A_{ij}$  sustained across all models (ER, SF, SF1, SF2) and relevant empirical networks (PPI1–PPI4, Brain). **b**, For  $\mathbb{R}_2$  and  $\mathbb{P}$  we predict  $\theta=3/2$  and  $\theta=1$ , respectively (solid lines), in perfect agreement with the observed results (symbols). **c**, For  $\mathbb{M}$  and  $\mathbb{E}$  we predict  $\theta=-1$ , again confirmed for both the model and relevant empirical networks. **d**,  $T(j \rightarrow i)$  versus  $L_{ij}$  as obtained from  $\mathbb{R}_1$  and  $\mathbb{N}$  on ER and SF. These systems are in the distance-limited regime,  $\theta=0$ , in which  $T(j \rightarrow i)$  is proportional to  $L_{ij}$ . **e**,  $\mathbb{R}_2$  and  $\mathbb{P}$ , having  $\theta>0$ , are in the degree-limited regime, and consequently  $T(j \rightarrow i)$  is almost independent of  $L_{ij}$ . **f**,  $\mathbb{M}$  and  $\mathbb{E}$  represent composite dynamics, where, again  $T(j \rightarrow i) \propto L_{ij}$ . **g–i**, The mean propagation time  $\langle T \rangle$  on ER and SF networks with identical average degree  $\langle S \rangle$ . **g**, Distance limited:  $\langle T \rangle$  is unaffected by the ER/SF networks, other than a minor decrease in  $\langle T \rangle$  for SF, a consequence of the typically shorter paths characterizing SF networks. **h**, Degree limited: here hubs delay the propagation, and hence SF dramatically increases  $\langle T \rangle$ . The effect is more pronounced when  $\theta$  is large. Indeed,  $\mathbb{R}_2$  ( $\theta=3/2$ ) features a 612% increase, compared with the 278% exhibited by  $\mathbb{P}$  ( $\theta=1$ ). **i**, Composite:  $\langle T \rangle$  is dominated by the response time of the small nodes, which is roughly the same in ER and SF. It is smaller than in the two other regimes (blue, red) due to the fast response of the hubs along all pathways from source to target. **j**, Efficient spread:  $\langle T \rangle$  versus the number of nodes  $N$  as obtained from  $\mathbb{R}_1$  (dark) and  $\mathbb{N}$  (light). As predicted,  $\langle T \rangle \sim \log N$  (solid lines). **k**, Slow spread: for  $\mathbb{R}_2$  (dark) and  $\mathbb{P}$  (light),  $\langle T \rangle \sim N^\alpha$  (solid line represents  $\alpha=1/2$ ). Hence, despite the fact that SF shrinks the mean topological distance  $\langle L \rangle$ , it greatly inflates the mean temporal distance  $\langle T \rangle$ . **l**, Ultra-efficient spread: in composite dynamics we predict  $\langle T \rangle \sim \text{const}$ , independent of system size. Indeed,  $N$  spans four orders of magnitude, whereas  $\langle T \rangle$  is practically constant. Data points in **a–c** and **j–l** represent logarithmic bins<sup>44</sup> in  $S_i, N$  (Supplementary Section 3.3).

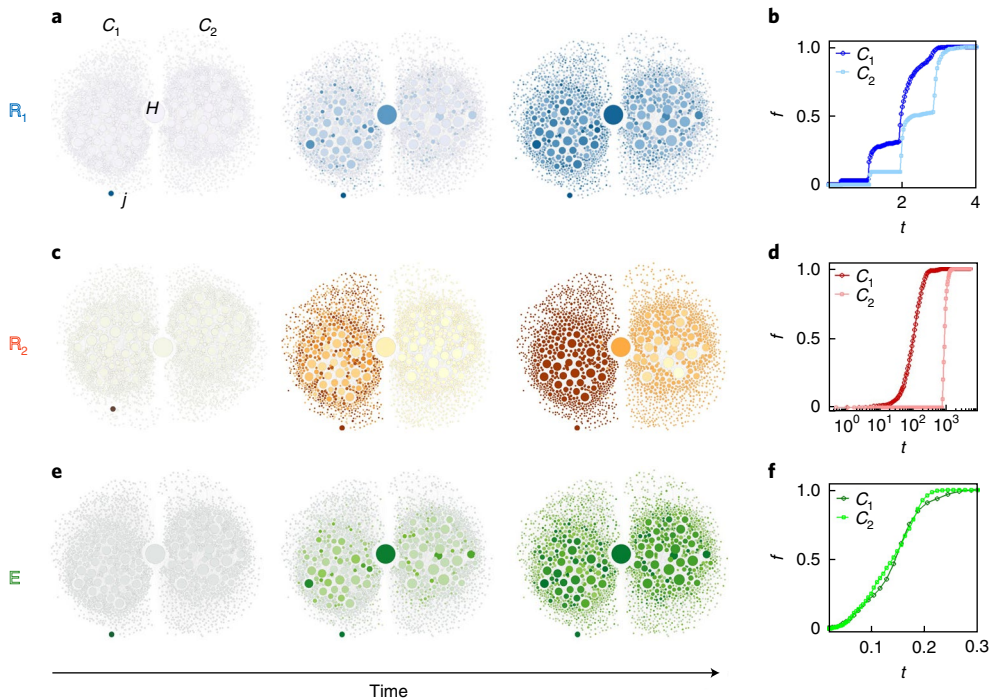


**Fig. 5 | Propagation between communities (see Methods).** We constructed a modular network with two SF communities,  $C_1$  and  $C_2$ , comprising  $N=1,000$  nodes each, linked by a single hub  $H$ . At  $t=0$  we introduced a signal on a source node  $j \in C_1$  (blue node at bottom left), then tracked the propagation across the communities. **a**, Distance-limited  $\mathbb{R}_1$ . As expected the signal first impacts nodes in  $C_1$ , then spills over to  $C_2$  through  $H$ . **b**, The fraction  $f$  of nodes impacted by the signal versus  $t$  for  $C_1$  (dark) and  $C_2$  (light) for the case in **a**. A node  $i$  is considered to be impacted at time  $t$  if  $T(j \rightarrow i) \leq t$ . Nodes in  $C_2$  show a slightly delayed response compared with  $C_1$ , owing to the typically longer cross-community pathways. The observed step-like propagation pattern reflects the discrete nature of the network paths, which govern the advancement of signals in the distance-limited regime (as also expressed through the discrete peaks of  $P(T)$  in this dynamic family; Fig. 3g,h). **c**, Degree-limited  $\mathbb{R}_2$ . Here the slow responding hub serves as a shock absorber, and hence the signal remains confined to  $C_1$  for a long time. Therefore, in this class topological modularity is amplified, translating into a strong dynamic modularity. **d**,  $f$  versus  $t$  for the case in **c** shows that, indeed, the spillover to  $C_2$  is extremely delayed, occurring orders of magnitude later than the complete response of  $C_1$  ( $f \rightarrow 1$ , dark red). **e,f**, Composite  $\mathbb{E}$ . In this class hubs respond extremely fast, rendering the community boundaries ( $H$ ) effectively transparent for dynamic signal propagation. As a result  $C_1$  and  $C_2$  respond in unison, showing almost no dynamic traces associated with the topological modularity.

Going beyond the averaged  $\langle T \rangle$ , a most profound distinction between the three regimes is expressed through the response time distribution,  $P(T)$ , capturing the probability density that a randomly selected  $i, j$  pair has  $T(j \rightarrow i) \in (T, T + dT)$ . In the distance-limited regime, nodes are divided into discrete equidistant shells, comprising the nearest neighbours of the signal source, the next-nearest neighbours and so on. In each of these shells, the signal reaches all nodes approximately simultaneously, resulting in discrete time intervals, which shape  $P(T)$  in a unique form of sequentially separated peaks, a distinctive structure that can be observed in Fig. 3g,h. Here, since response time is independent of degree, we predict that the structure of  $P(T)$  is unaffected by  $P(S)$ , and hence ER (top) and SF (bottom) have similar  $P(T)$ . In contrast, under degree-limited propagation, SF networks exhibit a much broader  $P(T)$ , a consequence of the delayed propagation caused by the hubs (Fig. 3i,j). With  $P(S)$  being the prime determinant of the propagation in this regime, the discrete nature of  $L_{ij}$ , responsible for the peaks in the distance-limited  $P(T)$ , now plays no role in shaping the system's temporal response patterns. Finally, in composite dynamics,  $P(T)$  is shaped by both  $L_{ij}$  and  $P(S)$ , leading to a sequence of overlapping peaks (Fig. 3k,l). This captures the essence of the composite regime: the mean propagation time is governed by  $L_{ij}$  (peaks), whereas at each distance, the variance is governed by  $P(S)$  (width of each peak), a composition of degrees and distances. Hence, our predicted regimes ( $\theta$  positive, negative or zero) are characterized by highly distinctive  $P(T)$ , providing a clear fingerprint for each of the predicted propagation patterns.

In Fig. 5 we illustrate the impact of network modularity on signal propagation in each of our three dynamic regimes (see Methods).

Taken together, we find that the zoo of diverse spreading behaviours observed in Figs. 1–5 is, in fact, a consequence of a deep universality that can be fully predicted through the single, analytically tractable, exponent  $\theta$ . Its value helps systematically translate microscopic ( $S_i$ ), mesoscopic ( $L_{ij}$ , modularity) and macroscopic ( $P(S)$ ,  $N$ ) network characteristics into distinctive patterns of dynamic propagation, all summarized in Fig. 2e.

#### Universal dynamic metric for signal propagation

To simplify the observed signal propagation we seek a predictive metric,  $\mathcal{L}(j \rightarrow i)$  that transparently reflects the actual propagation times  $T(j \rightarrow i)$ ; namely we seek a temporal distance  $\mathcal{L}(j \rightarrow i) \propto T(j \rightarrow i)$  (ref. <sup>1</sup>). Consider the shortest path  $\Pi(j \rightarrow i) = j \rightarrow q \rightarrow \dots \rightarrow i$  from the source  $j$  to the target  $i$ . Being shortest, this path is the main artery through which  $j$ 's signal impacts  $i$  (ref. <sup>4</sup>). Following equation (4), the delay incurred on each node  $p \in \Pi(j \rightarrow i)$  scales as  $S_p^\theta$ , therefore leading to the desired metric

$$\mathcal{L}(j \rightarrow i) = \min_{\Pi(j \rightarrow i)} \left\{ \sum_{\substack{p \in \Pi(j \rightarrow i) \\ p \neq j}} S_p^\theta \right\}. \quad (7)$$

The summation captures the accumulated lag time along each path, and the minimization selects the fastest of all shortest paths from  $j$

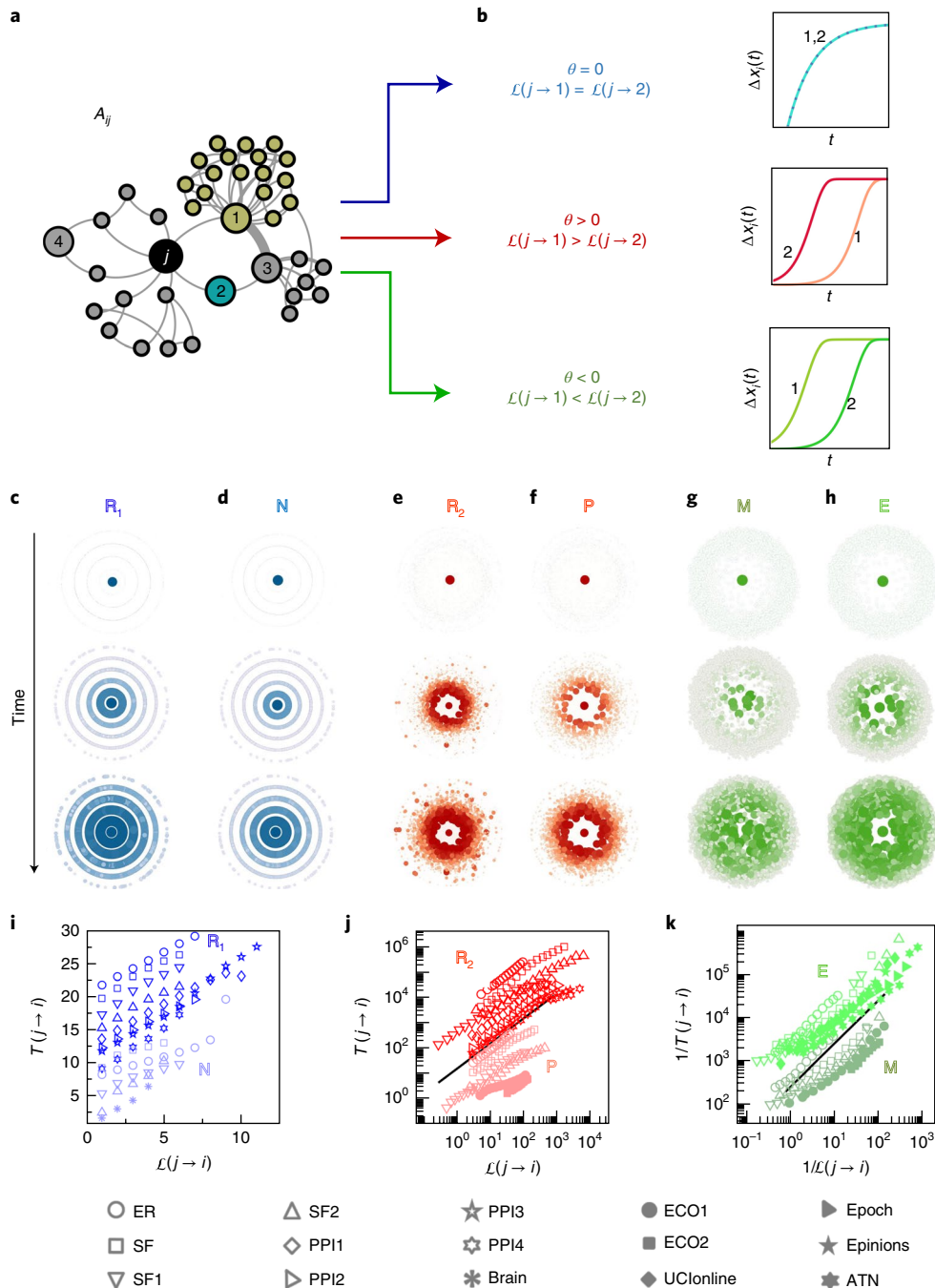


**Fig. 6 | The universal temporal distance  $L(j \rightarrow i)$ .** **a**, The signal travelling from  $j$  (black) will feature different spreading patterns under different dynamics, which we capture through  $L(j \rightarrow i)$ . **b**, The signal will impact 1 and 2, both at topological distance  $L_1 = L_2 = 1$ , simultaneously if the dynamics is distance limited (top, blue); 2 before 1 under degree-limited propagation (centre, red) due to the delayed response of the hubs, and 1 before 2 in composite dynamics (bottom, green). In all cases, the temporal distance  $L(j \rightarrow i)$  in equation (7) is designed to locate 1 and 2, as well as all other nodes, at the appropriate distance from  $j$ , depending on the propagation regime. **c–h**, We used  $L(j \rightarrow i)$  to layout the nodes in each of our 41 test systems (detailed in Fig. 2), here re-displaying the original layouts of Fig. 3a–f. The unpredictable and inconsistent behaviour—that is, the zoo of Fig. 3—transforms into a well-organized concentric propagation pattern, in which the distance from the source naturally captures the actual travel time of the propagating signal. These layouts locate all nodes differentially, according to the system’s dynamics. For  $R_1$  and  $N$  (blue) nodes are condensed into separated shells, corresponding to the discrete nature of  $L_{ij}$  (peaks in  $P(T)$ , Fig. 3g,h). In  $R_2$  and  $P$  (red) the hubs become bottlenecks, and hence  $L(j \rightarrow i)$  assigns a larger distance to paths enriched with hubs. Conversely, in  $M$  and  $E$ ,  $L(j \rightarrow i)$  places the slower low-degree nodes in the network periphery and shifts hubs towards the centre. Additional layouts from our empirical networks are shown in Supplementary Section 4. **i**,  $T(j \rightarrow i)$  versus  $L(j \rightarrow i)$  for all networks under the distance-limited  $R_1$  (dark) and  $N$  (light) dynamics. The linear relationship indicates that  $L(j \rightarrow i)$  precisely captures the actual patterns of propagation. **j**,  $T(j \rightarrow i)$  versus  $L(j \rightarrow i)$  in the degree-limited  $R_2$  (dark) and  $P$  (light). Here  $T(j \rightarrow i)$  and  $L(j \rightarrow i)$  span several orders of magnitude, hence we use a logarithmic scale (black solid line represents a linear slope). **k**, For  $M$  (dark) and  $E$  (light)  $L(j \rightarrow i)$  and  $T(j \rightarrow i)$  inversely scale with the weighted degrees of nodes along each path. Therefore we use inverted axes  $1/T(j \rightarrow i)$  versus  $1/L(j \rightarrow i)$ . In **j** and **k** we employed logarithmic binning<sup>44</sup> (Supplementary Section 3.3).

to  $i$ . Equation (7) provides the temporal distance between all pairs of nodes  $i$  and  $j$ , designed to naturally capture the system's dynamic signal propagation. As opposed to other common metrics,  $\mathcal{L}(j \rightarrow i)$  depends not only on  $A_{ij}$  but also on the dynamics  $\mathbf{M}$  through  $\theta$  (equation (5)). Hence, for a given  $A_{ij}$  the distances  $\mathcal{L}(j \rightarrow i)$  are adaptive, relocating all nodes depending on the nature of the system's nonlinear interactions (Fig. 6a,b).

To test equation (7) we used it to layout the SF networks shown in Fig. 3a–f, placing each node in its appropriate location, at distance  $\mathcal{L}(j \rightarrow i)$  from the perturbed source (Fig. 6c–h). The originally unpredictable spreading patterns (Fig. 3) collapse into a concentric propagation, with the desired  $T(j \rightarrow i) \propto \mathcal{L}(j \rightarrow i)$ . The crucial point is that these layouts are dynamically adaptive. Hence, despite using the same  $A_{ij}$  the nodes are located differently as the dynamics is shifted from  $\mathbb{R}_1$  and  $\mathbb{N}$  (blue,  $\theta=0$ ) to  $\mathbb{R}_2$  and  $\mathbb{P}$  (red,  $\theta=1, 3/2$ ), and further to  $\mathbb{M}$  and  $\mathbb{E}$  (green,  $\theta=-1$ ). In Fig. 6i–k we show the observed  $T(j \rightarrow i)$  versus the analytically calculated  $\mathcal{L}(j \rightarrow i)$  in equation (7) for all our 41 model/empirical systems—each according to its classification (blue, red, green). Layouts of all remaining systems appear in Supplementary Section 4.

**Extended testing.** In Supplementary Sections 5 and 6 we examine the application of our formalism to two real systems, capturing the spread of a global epidemic, and the propagation of a power cascade. We further discuss the empirical relevance of our framework in Supplementary Sections 7 and 8. These applications and tests go beyond our analytical framework; therefore, they help us examine the relevance and applicability of our general approach: to first map the timescales associated with individual components ( $\tau_i$ ), and then piece them together to obtain the global propagation patterns (for example,  $P(T), \mathcal{L}(j \rightarrow i)$ ).

## Discussion and outlook

Predicting the spread of information in a complex network environment is at the heart of our ability to understand its dynamic behaviour, hence the widespread efforts to collect data on the topology of real biological, social and technological networks. Yet, if we wish to leverage these data into actual dynamic insights, we must systematically translate our findings on network structure into dynamic predictions. Our formalism offers such translation by separating the contribution of the topology,  $A_{ij}$ , from that of the dynamics,  $\mathbf{M}$ , using the exponent  $\theta$  to obtain the different forms in which  $A_{ij}$  generates signal propagation.

A crucial aspect of our predicted propagation patterns is that they are fully controlled by the system's dynamics, independent of the underlying topology. Therefore, being, for example, in the composite class is an intrinsic fingerprint of the SIS model  $\mathbb{E}$ , regardless of whether it is implemented on Epoch or on UCIonline. Interestingly, within the same dynamics, the propagation class may, generally, change as the system transitions between states. For example, in Supplementary Section 7.6 we show that the pandemic transition in  $\mathbb{E}$  is also a transition from distance-limited to composite dynamics. This offers an additional layer by which to understand such state transitions: the system not only transfers from healthy to pandemic, but also changes its propagation regime.

Although complex system dynamics can take almost unlimited forms, our formalism shows that the determinants of information spread are restricted to the few leading powers of  $\mathbf{M}$ , as encapsulated within  $\Gamma(0)$  in equation (6). This groups together fundamentally different dynamics under the same propagation class, for example, ecological interactions ( $\mathbb{M}$ ) and epidemics ( $\mathbb{E}$ ), which exhibit identical spreading patterns. Most importantly, the dependence on the powers ( $\Gamma(n)$ ) as opposed to the coefficients ( $C_n$ ), shows that our predictions are intrinsic to the system's dynamics, determined by the functional form of  $\mathbf{M}$ , rather than by its specific rate constants. For instance, our prediction that  $\mathbb{E}$  is in the composite regime is not

sensitive to the microscopic rates of infection/recovery, which vary across different diseases, but rather represents a robust property of the SIS model itself. Hence  $\theta$  reduces the complexity of the microscopic description to a small number of relevant parameters—here the leading powers of  $\mathbf{M}$ . An analogous approach was successfully employed in the past to expose universality in particle systems<sup>37</sup> and we believe that this line of thought may lead to similar breakthroughs in our understanding of complex network dynamics.

## Online content

Any methods, additional references, Nature Research reporting summaries, source data, statements of data availability and associated accession codes are available at <https://doi.org/10.1038/s41567-018-0409-0>.

Received: 25 September 2017; Accepted: 13 December 2018;  
Published online: 28 January 2019

## References

- Brockmann, D. & Helbing, D. The hidden geometry of complex, network-driven contagion phenomena. *Science* **342**, 1337–1342 (2013).
- Kumar, J., Rotter, S. & Aertsen, A. Spiking activity propagation in neuronal networks: reconciling different perspectives on neural coding. *Nat. Rev. Neurosci.* **11**, 615–627 (2010).
- Maslov, S. & Ispolatov, I. Propagation of large concentration changes in reversible protein-binding networks. *Proc. Natl Acad. Sci. USA* **104**, 13655–13660 (2007).
- Barzel, B. & Barabási, A.-L. Universality in network dynamics. *Nat. Phys.* **9**, 673–681 (2013).
- Barzel, B., Liu, Y.-Y. & Barabási, A.-L. Constructing minimal models for complex system dynamics. *Nat. Commun.* **6**, 7186 (2015).
- Holter, N. S., Maritan, A., Cieplak, M., Fedoroff, N. V. & Banavar, J. R. Dynamic modeling of gene expression data. *Proc. Natl Acad. Sci. USA* **98**, 1693–1698 (2001).
- Afraimovich, V. S. & Bunimovich, L. A. Dynamical networks: interplay of topology, interactions and local dynamics. *Nonlinearity* **20**, 1761–1771 (2007).
- Kirst, C., Timme, M. & Battaglia, D. Dynamic information routing in complex networks. *Nat. Commun.* **7**, 11061 (2016).
- Barat, A., Barthélémy, M. & Vespignani, A. *Dynamical Processes on Complex Networks* (Cambridge Univ. Press, Cambridge, 2008).
- Gao, J., Barzel, B. & Barabási, A.-L. Universal resilience patterns in complex networks. *Nature* **530**, 307–312 (2016).
- Harush, U. & Barzel, B. Dynamic patterns of information flow in complex networks. *Nat. Commun.* **8**, 2181 (2017).
- Kauffman, S. The ensemble approach to understand genetic regulatory networks. *Physica A* **340**, 733–740 (2004).
- Barzel, B. & Biham, O. Quantifying the connectivity of a network: the network correlation function method. *Phys. Rev. E* **80**, 046104 (2009).
- Crucitti, P., Latora, V. & Marchiori, M. Model for cascading failures in complex networks. *Phys. Rev. E* **69**, 045104 (2004).
- Dobson, I., Carreras, B. A., Lynch, V. E. & Newman, D. E. Complex systems analysis of series of blackouts: cascading failure, critical points, and self-organization. *Chaos* **17**, 026103 (2007).
- Voit, E. O. *Computational Analysis of Biochemical Systems* (Cambridge Univ. Press, New York, NY, 2000).
- Alon, U. *An Introduction to Systems Biology: Design Principles of Biological Circuits* (Chapman & Hall, London, 2006).
- Karlebach, G. & Shamir, R. Modelling and analysis of gene regulatory networks. *Nat. Rev. Genet.* **9**, 770–780 (2008).
- Barabási, A.-L. & Albert, R. Emergence of scaling in random networks. *Science* **286**, 509–512 (1999).
- Opsahl, T. & Panzarasa, P. Clustering in weighted networks. *Soc. Networks* **31**, 155–163 (2009).
- Eckmann, J.-P., Moses, E. & Sergi, D. Entropy of dialogues creates coherent structures in e-mail traffic. *Proc. Natl Acad. Sci. USA* **101**, 14333–14337 (2004).
- Ikehara, K. & Clauset, A. Characterizing the structural diversity of complex networks across domains. Preprint at <https://arXiv.org/abs/1710.11304v1> (2017).
- Yu, H. et al. High-quality binary protein interaction map of the yeast interactome network. *Science* **322**, 104–110 (2008).
- Rual, J. F. et al. Towards a proteome-scale map of the human protein-protein interaction network. *Nature* **437**, 1173–1178 (2005).
- Sporns, O., Tononi, G. & Kötter, R. The human connectome: a structural description of the human brain. *PLoS Comput. Biol.* **1**, e42 (2005).

26. Robertson, C. *Flowers and Insects: Lists of Visitors of Four Hundred and Fifty-three Flowers* (C. Robertson, Carlinville, IL, 1929).
27. Pastor-Satorras, R., Castellano, C., Van Mieghem, P. & Vespignani, A. Epidemic processes in complex networks. *Rev. Mod. Phys.* **87**, 925–958 (2015).
28. Stern, M., Sompolinsky, H. & Abbott, L. F. Dynamics of random neural networks with bistable units. *Phys. Rev. E* **90**, 062710 (2014).
29. Gardiner, C. W. *Handbook of Stochastic Methods* (Springer-Verlag, Berlin, 2004).
30. Castellano, C., Fortunato, S. & Loreto, V. Statistical physics of social dynamics. *Rev. Mod. Phys.* **81**, 591–646 (2009).
31. Hayes, J. F. & Ganesh Babu, T. V. J. *Modeling and Analysis of Telecommunications Networks* (John Wiley & Sons, Inc, Hoboken, 2004).
32. Kuramoto, Y. *Chemical Oscillations, Waves and Turbulence* (Springer-Verlag, Berlin, Heidelberg, 1984).
33. Newman, M. E. J. *Networks - An Introduction* (Oxford Univ. Press, New York, 2010).
34. Schmetterer, L. & Sigmund, K. (eds) *Hans Hahn Gesammelte Abhandlungen Band 1/Hans Hahn Collected Works Vol. 1* (Springer, Vienna, Austria, 1995).
35. Cohen, R. & Havlin, S. Scale-free networks are ultrasmall. *Phys. Rev. Lett.* **90**, 058701 (2003).
36. Caldarelli, G. *Scale-free Networks: Complex Webs in Nature and Technology* (Oxford Univ. Press, New York, 2007).
37. Wilson, K. G. The renormalization group: critical phenomena and the Kondo problem. *Rev. Mod. Phys.* **47**, 773 (1975).
38. Bullmore, E. & Sporns, O. Complex brain networks: graph theoretical analysis of structural and functional systems. *Nat. Rev. Neurosci.* **10**, 186–198 (2009).
39. Wai, H.-T., Scaglione, A., Harush, U., Barzel, B. & Leshem, A. RIDS: robust identification of sparse gene regulatory networks from perturbation experiments. Preprint at <https://arxiv.org/abs/1612.06565> (2017).
40. Novozhilov, A. S., Karev, G. P. & Koonin, E. V. Biological applications of the theory of birth-and-death processes. *Brief. Bioinform.* **7**, 70–85 (2006).
41. Hufnagel, L., Brockmann, D. & Geisel, T. Forecast and control of epidemics in a globalized world. *Proc. Natl Acad. Sci. USA* **101**, 15124–15129 (2004).
42. Pastor-Satorras, R. & Vespignani, A. Epidemic spreading in scale-free networks. *Phys. Rev. Lett.* **86**, 3200–3203 (2001).
43. Dodds, P. S. & Watts, D. J. A generalized model of social and biological contagion. *J. Theor. Biol.* **232**, 587–604 (2005).
44. Milojević, S. Power-law distributions in information science: making the case for logarithmic binning. *J. Am. Soc. Inf. Sci. Technol.* **61**, 2417–2425 (2010).

## Acknowledgements

C.H. thanks the Planning and Budgeting Committee (PBC) of the Council for Higher Education, Israel, and the INSPIRE-Faculty grant (code: IFA17-PH193) for support. This work was supported by the US National Science Foundation-CRISP award no. 1735505, the BIU Center for Research in Applied Cryptography and Cyber Security in conjunction with the Israel National Directorate in the Prime Minister's office, and by a grant from the Ministry of Science & Technology, Israel & Ministry of Foreign Affairs and International Cooperation General Directorate for Country Promotion, Italian Republic.

## Author contributions

All authors designed and conducted the research. C.H. and U.H. analysed the data and performed the numerical simulations. B.B. was the lead principal investigator.

## Competing interests

The authors declare no competing interests.

## Additional information

**Supplementary information** is available for this paper at <https://doi.org/10.1038/s41567-018-0409-0>.

**Reprints and permissions information** is available at [www.nature.com/reprints](http://www.nature.com/reprints).

**Correspondence and requests for materials** should be addressed to B.B.

**Publisher's note:** Springer Nature remains neutral with regard to jurisdictional claims in published maps and institutional affiliations.

© The Author(s), under exclusive licence to Springer Nature Limited 2019

## Methods

**Derivation outline for the universal exponent  $\theta$ .** Although a detailed and rigorous derivation is provided in Supplementary Section 1, here we provide a rough derivation, outlining the main steps used to derive equations (4) and (5). First we write equation (3) as

$$\frac{dx_i}{dt} = M_0(x_i(t)) + S_i M_1(x_i(t)) \mathcal{M}_i(t) \quad (8)$$

where  $S_i = \sum_{j=1}^N A_{ij}$  is node  $i$ 's weighted degree, and

$$\mathcal{M}_i(t) = \frac{1}{S_i} \sum_{j=1}^N A_{ij} M_2(x_j(t)) \quad (9)$$

represents the mean impact experienced by node  $i$  from its direct neighbourhood. Under the configuration model framework, node  $i$ 's neighbours are extracted from a similar distribution to that of all other nodes, allowing us to substitute  $\mathcal{M}_i(t)$  by  $\mathcal{M}(t)$ , omitting the index  $i$ , to signify the fact that, on average,  $i$ 's neighbourhood is identical to that of all other nodes (Supplementary Section 1.1). Using this approximation in equation (8), and setting the derivative on the left-hand-side to zero we obtain the steady-state activities of all nodes

$$x_i = R^{-1}(\lambda_i) \quad (10)$$

where  $R(x) = -M_1(x)/M_0(x)$ ,  $\lambda_i = 1 / M S_i \propto S_i^{-1}$  and  $R^{-1}(x)$  represents  $R$ 's inverse function (Supplementary Section 1.2). Omitting the argument  $t$ , we use  $x_i$  and  $\mathcal{M}$  to denote the steady-state values of  $x_i(t)$  and  $\mathcal{M}(t)$ . Next we consider the response  $\Delta x_i(t)$  of equation (8) to a small perturbation  $\Delta x_m$  to one of  $i$ 's nearest neighbours, which, linearizing around the steady state, yields the non-homogeneous linear equation (Supplementary Section 1.3)

$$\frac{d\Delta x_i}{dt} = -\frac{1}{\tau_i} \Delta x_i(t) + f(S_p t) + O(\Delta x^2) \quad (11)$$

with

$$\tau_i = -\frac{1}{M'_0(x_i) + S_i M'_1(x_i) \mathcal{M}} \quad (12)$$

In equation (11)  $\tau_i$  represents node  $i$ 's intrinsic response time, which is precisely what we seek. In contrast, the non-homogeneous term  $f(S_p t)$  determines  $i$ 's final response  $\Delta x_i(t \rightarrow \infty)$ , but has no impact on its temporal dynamics towards this final state; hence in the present discussion we do not pursue this term any further (see Supplementary Section 1.3 for a more detailed treatment). The derivatives  $M'_q(x_i)$  ( $q=0, 1$ ) represent  $dM_q/dx$ , with  $x_i$  taken at the steady state, as provided by equation (10). Using the fact that  $M_0(x) = -M_1(x)/R(x)$  we write

$$\begin{aligned} M'_0(x_i) &= \left. \left( -\frac{M'_1(x_i)}{R(x_i)} + \frac{M_1(x_i)}{R^2(x_i)} R'(x_i) \right) \right|_{x_i=R^{-1}(\lambda_i)} \\ &= -\frac{M'_1(R^{-1}(\lambda_i))}{\lambda_i} + \frac{M_1(R^{-1}(\lambda_i)) R'(R^{-1}(\lambda_i))}{\lambda_i^2} \end{aligned} \quad (13)$$

where in the last step we used the fact that  $R(R^{-1}(\lambda_i)) = \lambda_i$ . In a similar fashion we express the second term in the denominator of equation (12) as

$$S_i M'_1(x_i) \mathcal{M} = \mathcal{M} \frac{M'_1(R^{-1}(\lambda_i))}{\lambda_i} \quad (14)$$

Collecting all terms we rewrite equation (12), preserving only the components that contribute to the scaling of  $\tau_i$  with  $S_i$  (or  $\lambda_i \propto S_i^{-1}$ ), ignoring, for instance, the nearest-neighbour average  $\mathcal{M}$ , which is independent of  $S_i$ . We arrive at

$$\frac{1}{\tau_i} \sim \frac{1}{\lambda_i^2} [R(R^{-1}(\lambda_i)) M'_1(R^{-1}(\lambda_i)) + M_1(R^{-1}(\lambda_i)) R'(R^{-1}(\lambda_i))] \quad (15)$$

where, once again, we used  $\lambda_i = R(R^{-1}(\lambda_i))$  to extract the pre-factor of  $\lambda_i^{-2}$  on the right-hand-side. Interestingly, the terms in the square brackets are in the form of a product derivative, allowing us to further simplify equation (15) into

$$\frac{1}{\tau_i} \sim \frac{1}{\lambda_i^2} \left. \frac{d[M_1(x_i) R(x_i)]}{dx_i} \right|_{x_i=R^{-1}(\lambda_i)} \quad (16)$$

We can now write

$$\tau_i \sim \lambda_i^2 Y(R^{-1}(\lambda_i)) \quad (17)$$

where

$$Y(x) = \left( \frac{d[M_1(x) R(x)]}{dx} \right)^{-1} \quad (18)$$

In the limit of large  $S_i$  (small  $\lambda_i$ ) we express  $Y(R^{-1}(\lambda_i))$  in equation (17) as a Hahn series around  $\lambda_i=0$

$$Y(R^{-1}(\lambda_i)) = \sum_{n=0}^{\infty} C_n \lambda_i^{\Gamma(n)} \quad (19)$$

which, to leading order, provides us with  $\tau_i \sim \lambda_i^2 \lambda_i^{\Gamma(0)}$ . Substituting  $S_i^{-1}$  for  $\lambda_i$ , we arrive at the desired scaling relationship

$$\tau_i \sim S_i^\theta \quad (20)$$

where  $\theta = -2 - \Gamma(0)$ , as appears in equations (4) and (5).

Interestingly, the scaling exponent  $\theta$  is fully determined by the self-dynamic functions  $M_0(x_i)$  and  $M_1(x_i)$ , independent of the neighbours' function  $M_2(x_i)$ . This does not mean that propagation times are not affected by  $M_2(x_i)$ , only that the scaling relationship of equation (4) is not sensitive to this function. Indeed,  $M_2(x_i)$  does impact the response time  $\tau_i$  in equation (12) through  $\mathcal{M}$ , which approximates the steady-state value of  $\mathcal{M}_i(t)$  in equation (9). However, when seeking  $\theta$  we are not focused on the specific value of  $\tau_i$ , but rather on its scaling with  $S_i$ . Hence, although  $\mathcal{M}$  contributes to this specific value, being independent of  $i$ , it has no bearing on  $\tau_i$ 's scaling with  $S_i$ . This separation is enabled by the configuration model, which allows us to approximate  $\mathcal{M}_i(t) \approx \mathcal{M}(t)$ , relying on the vanishing correlation between  $i$ 's degree and that of its neighbours (Supplementary Section 1.1).

The expansion in equation (19) is defined if the dynamic functions  $\mathbf{M}$  can be expressed by a convergent Hahn series around  $R^{-1}(0)$ , excluding, for example, discontinuous threshold dynamics, which cannot be treated within the bounds of our analytic framework.

**Example: mutualistic dynamics  $\mathbb{M}$ .** To extract  $\theta$  for the  $\mathbb{M}$ -dynamics (Fig. 2b) we first write it as

$$\mathbf{M} = \left( x(1-x^2), x, \frac{x}{1+x} \right) \quad (21)$$

setting, for simplicity, all rate constants to unity. Here we have  $R(x) = -M_1(x)/M_0(x) = 1/(x^2 - 1)$ , and therefore

$$R^{-1}(x) \sim \left( \frac{x+1}{x} \right)^{\frac{1}{2}} \quad (22)$$

Next we use equation (18) to write

$$Y(x) = \left( \frac{d}{dx} \left( \frac{x}{x^2 - 1} \right) \right)^{-1} = -\frac{(x^2 - 1)^2}{1 + x^2} \quad (23)$$

Taking  $R^{-1}(x)$  from equation (22), the Hahn expansion in equation (19) takes the form

$$Y(R^{-1}(\lambda_i)) = Y \left( \left( \frac{\lambda_i + 1}{\lambda_i} \right)^{\frac{1}{2}} \right) = \frac{1}{\lambda_i + 2\lambda_i^2} = \lambda_i^{-1} - 2\lambda_i^0 + 4\lambda_i^1 + O(\lambda_i^2) \quad (24)$$

for which the leading power is  $\Gamma(0) = -1$ . As a result we predict, using equation (5), that  $\theta = -2 - \Gamma(0) = -1$ , a negative scaling, placing  $\mathbb{M}$  in the composite regime. A detailed analysis of this and all other models of Fig. 2b appears in Supplementary Section 2.

**The impact of modularity (Fig. 5).** Although our quantitative predictions are valid under the configuration model (that is, a random network), they can still offer qualitative insights on more general structures. As an illustrative example, we consider the effect of network modularity on signal propagation. We constructed two communities, linked through a single hub (Fig. 5), representing, topologically, two distinct functional modules<sup>45</sup>. The question is whether this topological modularity translates also to dynamic modularity; namely, are the two modules functionally isolated. Indeed, this strongly depends on the dynamic regime of the system, as the exponent  $\theta$  crucially impacts the efficiency of information transfer between the modules: in distance-limited propagation the signal first spreads within its own module, but then spills over to the neighbouring module within a short time, driven by the short paths linking across the modules (Fig. 5a,b, blue). In contrast, under degree-limited propagation the connecting hub responds extremely slowly, acting as an effective shock-absorber, which restricts the signal for a very long time within one module (Fig. 5c,d, red). Hence, in this regime the structural modularity translates into an equally stiff dynamic modularity. In composite

dynamics the picture is fundamentally different: the rapidly responding hub node, effectively renders the boundary between the two communities transparent for signal propagation. Therefore, counter-intuitively, signals cross community boundaries almost instantaneously (Fig. 5e,f, green).

### Data availability

All data and codes to reproduce the results presented here are freely accessible at <https://github.com/CRHENNS/Spatio-Temporal-/blob/master/README.md>.

Additional information is available from the corresponding author upon reasonable request. The only exception is the air-traffic network data, which the authors are restricted from sharing.

### References

45. Ravasz, E. B. & Barabási, A.-L. Hierarchical organization in complex networks. *Phys. Rev. E* **67**, 026112 (2003).